Journal of Structural Geology 31 (2009) 1084–1099

Contents lists available at ScienceDirect

Journal of Structural Geology

journal homepage: www.elsevier.com/locate/jsg

Dilatant plasticity in high-strain experiments on calcite–muscovite aggregates

C. Delle Piane [a,*,1], C.J.L. Wilson [b], L. Burlini [a]

[a] Geological Institute ETH, Sonneggstraee 5, CH-8092 Zurich, Switzerland
[b] School of Earth Sciences, The University of Melbourne, Victoria 3010, Australia

ARTICLE INFO

Article history:
Received 29 February 2008
Received in revised form
20 February 2009
Accepted 3 March 2009
Available online 13 March 2009

Keywords:
Calcite
Muscovite
Shear zones
Two-phase rocks
High strain
Ductile failure
Phase equilibria
Metamorphic reaction

ABSTRACT

Torsion experiments were performed on synthetic aggregates of calcite with a 50% volume of muscovite. The tests were performed at 627–727 °C with a confining pressure of 300 MPa at constant shear strain rates of 3×10^{-5}–3×10^{-4} s^{-1} on cylindrical samples with the starting foliation parallel and perpendicular to the cylinder axis. Both the foliation parallel and the foliation perpendicular experiments show similar stress–strain patterns, with an initial hardening stage followed by significant strain weakening (>60%) before a catastrophic rupture. Microstructural analysis shows that in low-strain experiments calcite grains are intensely twinned while muscovite grains appear slightly bent and kinked. Higher strains promote a segregation of the two phases with calcite forming thin layers of fine, dynamically recrystallized grains, which act as localized shear bands, while muscovite grains keep their original size and rotate assuming a strong shape preferred orientation. This strain localization of the calcite from an initially homogeneous rock produced catastrophic failure at moderate bulk shear strains ($\gamma \sim 3$). Localization of the strain first involved ductile deformation to produce a new calcite layering with fine dynamically recrystallized grains along which cavities nucleated. The orientation and kinematics of the cavities are comparable to R1 Riedel structures. All experiments on calcite–muscovite mixtures resulted in heterogeneous strain. In these torsion experiments chemical changes and crystallization of new phases (anorthite and kalsilite) are observed at 627 °C. Whereas, samples hot pressed or deformed in compression at 670 °C did not show such reactions or any localization. The effect of stress-field geometry and pore pressure upon mineral reactions is discussed. It is concluded that deformation-induced heterogeneous phase distributions caused local strength differences initiating strain localization in the calcite–muscovite mixtures, eventually leading to plastic failure.

1. Introduction

In naturally deformed marbles, sheet silicates are the predominant minerals that form the foliation (Herwegh and Jenni, 2001; Leiss and Molli, 2003) but in many cases marbles are dominated by a strong compositional layering where the mineral phases are differentiated into a fine compositional layering (Molli et al., 2000) through a process of strain localization. The strength of these composite marbles also depends on the strengths of the constituent phases and their geometric arrangement, all of which may change with progressive strain. Experimental studies suggest that strain localization rarely occurs in a mono-phase material even after deformation to very large shear strains (e.g. $\gamma_{max} = 50$, in the case of Carrara marble Barnhoorn et al., 2004). Only few experimental deformation studies have been performed on two-phase aggregates, for example those on quartz–muscovite (Tullis and Wenk, 1994) and on calcite–anhydrite (Bruhn and Casey, 1997; Bruhn et al., 1999) showed that there is no strain localization at the sample scale in small strain, compression experiments. In contrast large-strain experiments on calcite–halite (Jordan, 1985), calcite–quartz aggregates (Rybacki et al., 2003), and calcite–anhydrite aggregates (Barnhoorn et al., 2005) strain localization from initially homogeneous rocks has been described.

There have been numerous experimental studies of the deformation of single crystals of various mica compositions (Etheridge et al., 1973; Mares and Kronenberg, 1993), demonstrating that they are able to undergo basal slip. Mariani et al. (2006) experimentally deformed fine-grained aggregates of muscovite up to shear strain of 2 at temperatures between 300 and 700 °C at pore pressure conditions suppressing the onset of dehydroxylation reaction. The authors inferred deformation to have occurred by a mixture of brittle/frictional and crystal-plastic

* Corresponding author. Tel.: +61 8 6436 8716; fax: +61 8 6436 8555.
E-mail addresses: claudio.dellepiane@csiro.au (C. Delle Piane), cjlw@unimelb.edu.au (C.J.L. Wilson), luigi.burlini@erdw.ethz.ch (L. Burlini).
[1] Present address: CSIRO Petroleum Resources, Australian Resources Research Centre, 26 Dick Perry Avenue, Kensington 6151, Western Australia.

0191-8141/$ – see front matter © 2009 Elsevier Ltd. All rights reserved.
doi:10.1016/j.jsg.2009.03.005

processes with a distinct switch of mechanical response from strain rate independent to linearly viscous, below a shear strain rate of $1.4 \times 10^{-5}\,s^{-1}$. In addition, there have been several experimental studies of the effect of the mica volume percentage and orientation on the deformation of schists and gneisses under conditions where the micas are crystal-plastic but the other minerals (mostly quartz and feldspar) are brittle (Gottschalk et al., 1990; Shea and Kronenberg, 1993; Holyoke and Tullis, 2006). For instance the experiments of Shea and Kronenberg (1993) are all coaxial, at room temperature, 200 MPa confining pressure, and showed that after small amounts of axial shortening strain was localized in the mica rich zones with cataclasis of the quartzo-felspathic stronger phases. Similar features are described in the shear experiments of Holyoke and Tullis (2006) undertaken on gneiss at high temperatures (745 °C and 800 °C) and high confining pressures (1500 MPa). This produced an interconnection of the weaker biotites and stress concentrations and brittle failure in the stronger framework grains of quartz and feldspar. However, there is a paucity of experiments of two-phase aggregates that identifies the behaviour of the individual phases at high strains.

Many of the previous experimental studies on calcite aggregates, particularly Carrara marble, were obtained from coaxial compression and extension deformation experiments (e.g. Rutter, 1974, 1995; Schmid et al., 1980) where the maximum strains reached in the experiments are too small to result in steady-state deformation behaviour. Whereas, Pieri et al. (2001) and Barnhoorn et al. (2004), in large-strain torsion experiments, have achieved mechanical steady-state flow in Carrara marble. This involved deformation in the dislocation creep field with dynamic recrystallization starting at moderate strains ($\gamma \sim 1$). The accompanying strain weakening involves cycles of both subgrain rotation and grain boundary migration at approximately constant stress levels.

The important mechanical influence of a weak phase that may control creep during dynamic recrystallization has also been suggested as a mechanism for flow localization in crustal rocks (Rutter and Brodie, 1992; Handy, 1994; Handy et al., 1999). In this study we will investigate the mechanical influence and microstructural aspects related to strain localization using two-phase samples prepared from Carrara marble and a muscovite powder. Another mechanism that has been identified in this investigation is dilatant plasticity. Dilatant plasticity is known from deformation of metals and ceramics (Kassner and Hayes, 2003; Chokshi, 2005), where it limits the life of components that are subjected to high-temperature creep. The micromechanism for the generation of high-temperature dilatant pore spaces, which, in the ceramic literature are called microcavities, is related to diffusional grain boundary sliding. Here we present evidence for cavity nucleation, also known as cavitation, which accompanies a chemical reaction involving the muscovite and calcite.

This paper focuses on the rheology and microstructural evolution of a synthetic calcite rock where there is the addition of muscovite deformed to moderate temperatures of 600–727 °C and 300 MPa. Maximum bulk shear strains of about 4.5 were achieved before sudden shear failure and abrupt stress drop. Prior to failure strain localization and mechanical softening can be correlated to the formation of zones of reduced grain size and ductile deformation in the calcite. Using microstructural observations it will be shown that calcite is the weak phase. However, the rheology of the polyphase aggregate is significantly influenced by the addition of the muscovite and at large strains, phase transformations and void formation produce a mechanism of dilatant plastic flow. Finally, we address the question as to the role of muscovite in producing the mineralogical segregations that we see in many natural marbles. For it is often inferred, that the presence of sheet silicate minerals is one of the factors that contribute to the localization of deformation in zones of high-strain in natural rocks.

2. Experimental procedures

2.1. Starting material

We performed deformation experiments on 10 synthetic two-phase aggregates containing 50% volume muscovite and 50% volume calcite prepared following the procedure described by Schmidt et al. (2008). The calcite powder had a grain size ranging from 0.3 to 60 μm (average 10 μm); it was obtained from a block of Carrara marble described by Pieri et al. (2001). The muscovite, obtained from Minas Gerais, Brazil, was purchased as fine-grained platelets with average lengths ranging from 50 to 100 μm and with length to width aspect ratios of approximately 10:1. The powders were mechanically mixed and oven dried at 120 °C for 24 h and then cold pressed in stainless steel cylinders by stepwise filling and pressing of small portions (ca. 20 g) at the same load to achieve a homogeneous compaction. The pressing was done with an Enerpac-H-Frame 50-t-press up to a maximum stress of 400 MPa. The cold pressed samples were then annealed by hot-isostatically pressing (HIPing) at 170 MPa and 670 °C for 3 h to generate firm samples. The initial porosity of the HIPped material was calculated by difference between the geometrical volume of each sample and the volume measured with a helium pycnometer (AccuPyc 1330) and resulted in an average value of porosity of 20% (see Fig. 1(c)). The specimens used in the experiments were precision-ground from the larger sized HIPed sample (S27) to produce cylinders 12 mm in diameter and approximately 10 mm in length.

The calcite fraction in the starting material shows a wide grain size distribution ranging from ~10 μm to 80 μm. The different grain size fractions are homogeneously distributed. The larger calcite grains are frequently strongly twinned, and overall no significant shape preferred orientation can be observed (Fig. 1(e)). The muscovite fraction also shows a wide grain size distribution with maximum grain sizes of 100 μm. The grains have their basal planes oriented normal to the compression direction and are often bent and kinked (Fig. 1(a)). The texture of the muscovite fraction was probably produced from rigid body rotation during compaction prior to the HIPing process.

2.2. Deformation experiments

Deformation experiments were performed in a Paterson-type gas medium apparatus (Paterson and Olgaard, 2000) in torsion and in compression testing at 300 MPa confining pressure, temperatures between $T = 627$–727 °C (Table 1) under undrained conditions. The samples were constrained between alumina spacers and zirconia end pistons within an iron jacket of 0.25 mm wall thickness and 15 mm diameter. The temperature during an experiment was monitored using a K-type thermocouple placed at about 3 mm from the top of the sample and the gradient along the sample axis was ±1 °C. Two type of stress configuration were tested in order to assess the role of the three principal stresses orientation on the high temperature, high pressure chemical stability of the aggregate.

2.2.1. Torsion experiments

Torsion tests allow simple shear deformation configuration with σ_1 and σ_3 inclined at 45° to the axis of the cylindrical sample

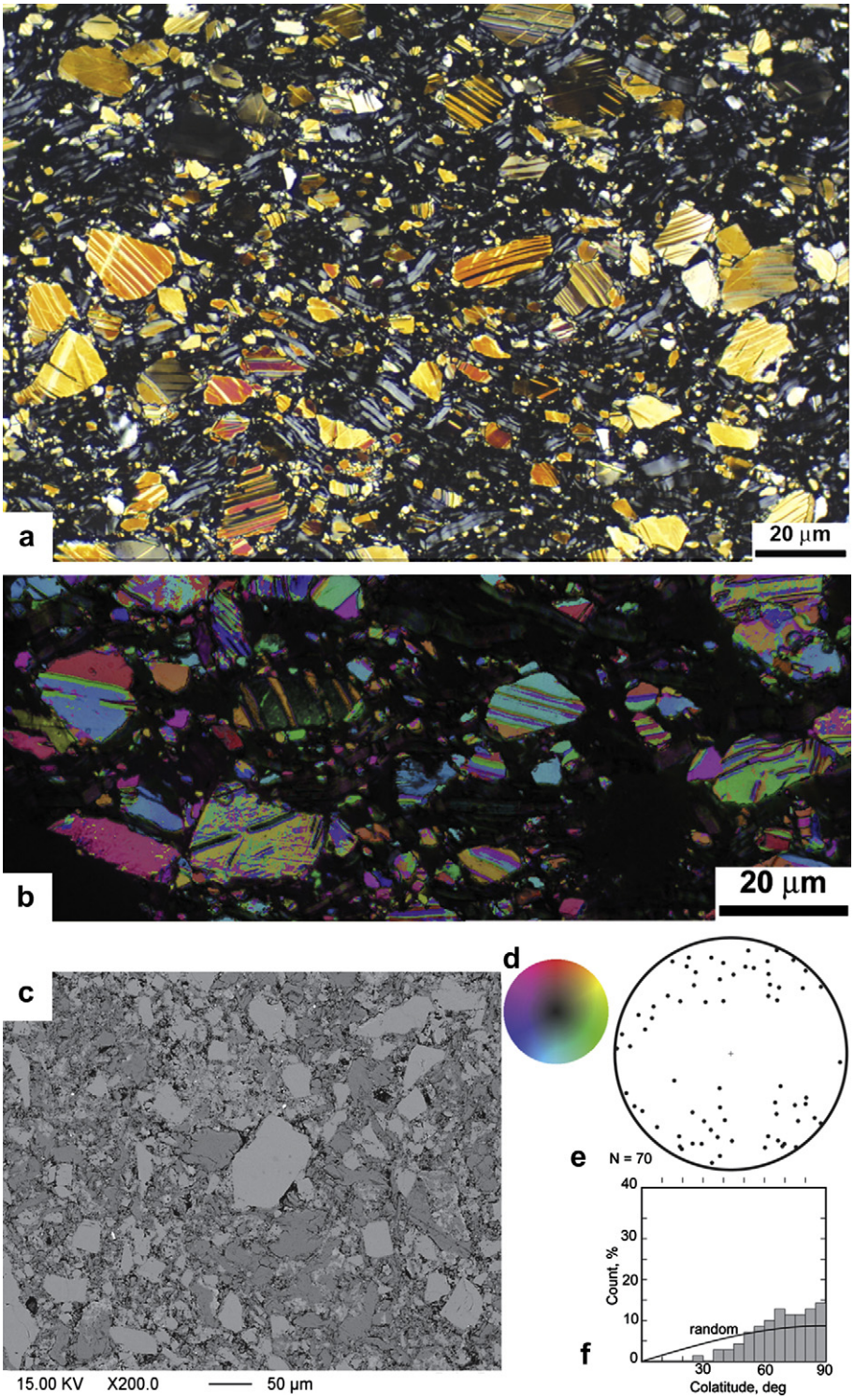

Fig. 1. Starting material microstructure and c-axis fabrics. (a) Photomicrograph in crossed polarized light of ultra-thin section showing distribution of calcite grains in muscovite matrix. (b) AVA image illustrating typical distribution of twinned calcite grains in a matrix of muscovite. (c) BSE image of the calcite–muscovite aggregates. Light grey is calcite, dark grey is muscovite, black is porosity. (d) The colour code relates to the three-dimensional c-axis orientation, namely the azimuth and plunge of the c-axis at each pixel seen in the AVA image of the calcite grains. (e) Lower hemisphere equal area stereonet plot showing the distribution of c-axes and number (N) of data points analysed. (f) Histogram showing frequency of grains whose c-axes occur at angle θ to the c-axis of adjacent grain, the curve represents a random distribution of c-axes.

(Paterson and Olgaard, 2000). A comprehensive description of the theoretical basis lying behind torsion testing can also be found in Handin et al. (1960).

Constant displacement rate experiments were performed with shear strain rates between 3×10^{-5} s^{-1} and 3×10^{-4} s^{-1} (Table 1). Due to strain-induced jacket failure, it was not possible to attain bulk shear strains higher than $\gamma \sim 4.5$. Thus the examination of microstructural evolution with strain was conducted comparing samples deformed at low and moderate strains with respect to highest strain attained.

Table 1
Sample geometry and experimental conditions of the calcite–muscovite experiments performed in torsion and compression. Values of strain rate are expressed in terms of bulk shear strain rate, and axial strain rate for the torsion and the compression experiments respectively. ⊥ = initial foliation perpendicular to the specimen cylindrical axis; // = initial foliation parallel to the specimen cylindrical axis.

Sample #	Diameter (mm)	Length (mm)	T (°C)	Confining pressure (MPa)	Bulk Strain	Strain rate (s^{-1})	Comments	Experiment type
PO752	11.99	11.33	727	300	~2.5	3×10^{-4}	⊥	Torsion
PO753	12.03	12.53	727	300	0.5	3×10^{-4}	⊥	
PO754	11.99	12.62	727	300	4.5	3×10^{-4}	⊥	
PO778	12.03	11.95	627	300	1	6×10^{-5}	⊥	
PO781	12.01	11.97	627	300	1	6×10^{-5}	⊥	
PO782	12.01	11.96	627	300	0.1	6×10^{-5}	⊥	
PO783	12.01	12.26	627	300	3	3×10^{-5}	⊥	
PO785	11.88	9.88	727	300	1.5	1×10^{-4}	//	
PO876	11.92	9.79	627	300	20%	4×10^{-4}	⊥	Compression

2.2.2. Compression experiments

In axial compression experiments $\sigma_2 = \sigma_3 =$ confining pressure while the maximum compressive principal stress σ_1 is oriented parallel to the cylinder axis.

Samples were shortened at nearly constant axial strain rates. Strain and strain rates were determined from measurements of axial displacement normalized to the original length of the specimen. Axial loads during compression were measured with an LVDT based internal load cell. The measured values were corrected taking into account the jacket strength, the rig distortion, the change in section size during deformation and then converted into differential stress (see Paterson and Olgaard, 2000).

2.3. Microstructural analysis

Microstructural analyses were carried out using light and electron microscopy. Optical thin sections (ca. 10 μm thick) were prepared mainly from cuts parallel to the torsion axis and tangential to the cylindrical surface (the "longitudinal tangential" position of Paterson and Olgaard, 2000). Such sections contain the direction of shear displacement and best illustrate the effects of the maximum shear strain. Crystallographic preferred orientation of the calcite grains were acquired using the Fabric Analyser described by Wilson et al. (2007), which allows a fast collection of high-resolution spatial c-axis orientation data from a set of digital polarized light images.

Backscatter electron (BSE) images obtained using a CamScan CS-44 LB scanning electron microscope (SEM) (acceleration voltage 15 kV, 20–13 mm working distance, and ~4 nA beam current), were used to visualize the pore and phase distribution and eventual reaction products in the deformed specimen. In addition characteristic X-ray radiations were collected and displayed as elemental maps to reveal the spatial distribution of specific elements. Elemental maps were acquired using an electron probe microanalyser (Jeol JXA-8200) at Institute of Mineralogy and Petrology of ETH using the following conditions: 11 mm working distance, 15 kV acceleration voltage, 4 nA probe current, 40 ms dwell time. Before the analyses each sample was ground and polished with diamond paste down to 1 μm and carbon coated to improve its electrical conductivity.

Ground powders of the deformed samples were analysed trough X-Ray Diffraction (XRD) to identify reaction products formed during the high-temperature experiments using a Powder X-ray diffractometer (Bruker, AXS D8 Advance), equipped with a Lynxeye superspeed detector.

3. Results

3.1. Mechanical data

The stress–strain curves relative to the torsion tests are illustrated in Fig. 2. All the experiments performed under torsion configuration showed a similar pattern: a quasi-linear elastic loading was followed by yielding and primary creep with strain hardening behaviour until shear strains of about $\gamma = 0.6$. With increasing shear strains the aggregates showed a remarkable weakening of up to 60% with respect to the peak torque. At bulk shear strain greater than $\gamma = 2$ the strength of the deforming aggregate shows minor fluctuations around a quasi-steady value of ca. 18 Nm. Large-strains experiments usually ended with catastrophic jacket failure.

The value of peak torque does not appear to be significantly affected by variation of displacement rate and temperature; this consideration and microstructural observation reported in the following section, led us to choose a high value of stress exponent ($n = 10$) when converting the measured torque M into shear stress (τ) as illustrated by Pieri et al. (2001), and Barnhoorn et al. (2004). The calculation was done following the equation reported by Paterson and Olgaard (2000):

$$\tau = \frac{(3 + \frac{1}{n})M}{2\pi R^3}$$

with R being the radius of the specimen.

The reproducibility of the torque for experiments performed at the same conditions of temperature, shear strain rate and pressure is within 3 Nm, which for a specimen of 12 mm diameter corresponds to 6.8 MPa.

The sample deformed in axial compression also showed a non-linear elastic loading followed by yielding at a differential stress of ca. 150 MPa. With increasing shortening the aggregate continuously hardens up to a maximum differential stress of 270 MPa reached at an axial strain of about 20%. The experiment was arbitrarily stopped at a maximum strain of 20% to avoid excessive distortion of the stress-field due to end-friction effects.

3.2. Strain gradients on the outer surface of the sample

Passive strain markers are drawn on the outer surface of the iron jacket containing the specimen to be deformed, in the form of straight thin scratches parallel to the cylinder axis. These lines are used to visualize eventual slip episodes at any of the interfaces between the different loading pistons, and also to picture the overall strain distribution at the outer diameter of a deformed specimen.

Low- to medium-strain torsion ($\gamma \leq 1$) experiments display a constant inclination of the reference scratches along the sample length. The angle between the normal to the cylinder axis and the strain markers, corresponds to the value of angular shear expected for the imposed shear strain.

Higher shear strain experiments show a significantly different pattern: the strain markers are inclined towards the sense of shear but their linear geometry is dissected by various discrete, thin

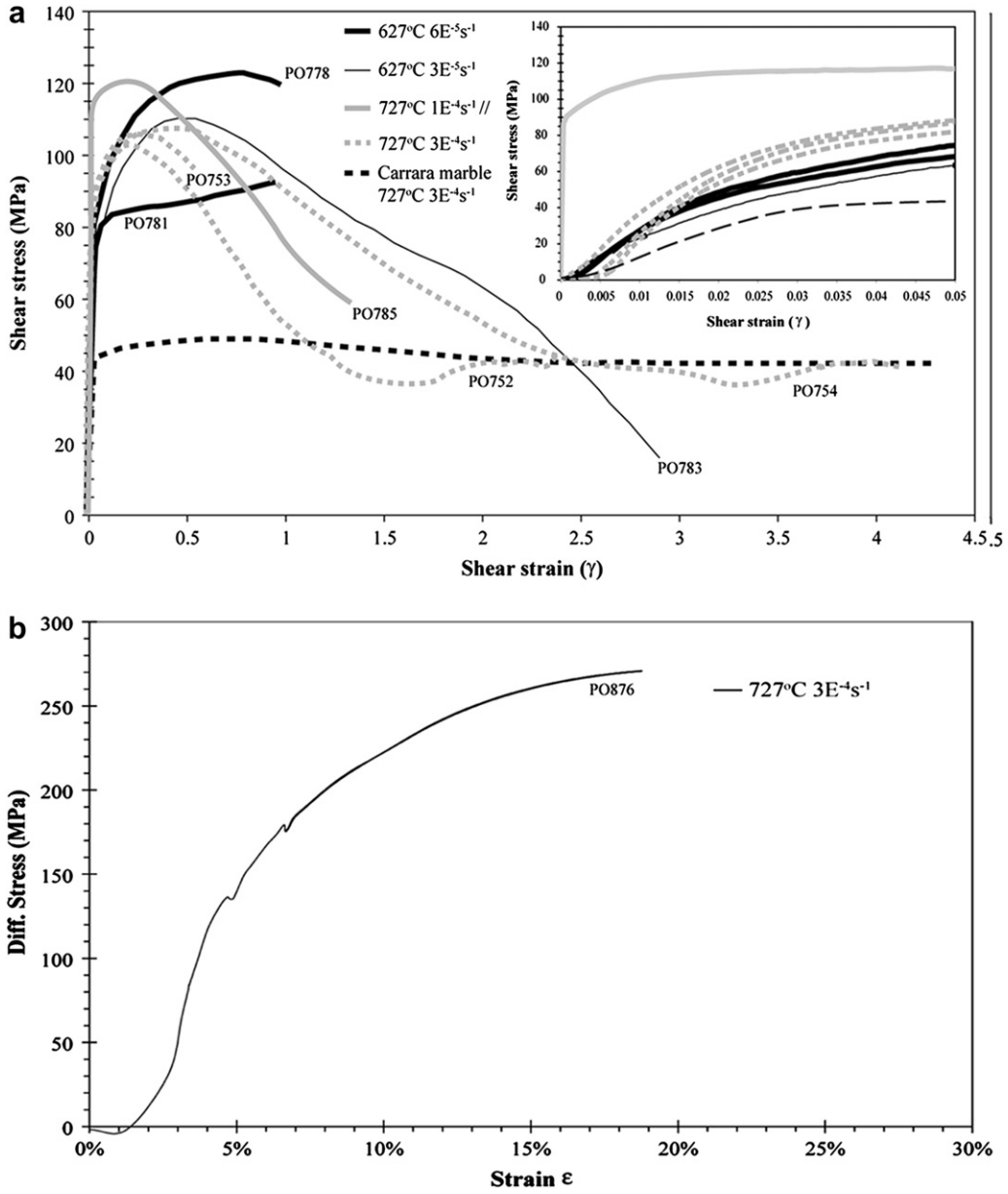

Fig. 2. Summary of the mechanical data for the performed experiments. (a). Shear stress versus bulk shear strain for experiments performed at 627 and 727 °C at various shear strain rates. Comparison with pure calcite Carrara marble (b). Mechanical behaviour in compression: differential stress in plotted as a function of the axial strain.

zones of concentrated shear, forming an acute angle against the shear direction (Fig. 3). The overall geometry of the intersecting linear features resembles that of an S–C′ mylonite with the S-foliation defined by the reference scratches, and the C′ folia corresponding to the planes of concentrated shear. Failure of the iron jacket systematically occurred within the latter.

3.3. Optical microstructures

At low- to medium-strains ($\gamma \leq 1$) and at $T = 627\,^{\circ}C$ calcite grains show widespread microstructural evidence of intracrystalline plasticity and there is no sign of obvious shear band development (Fig. 4(a)). The larger grains are intensely strained and display prominent undulose extinction, they are also twinned with twin lamellae exhibiting tapering edges and bent shapes; grain boundaries are normally straight or slightly curved (Fig. 4(a) and (b)). With increasing shear strain ($\gamma = 3$) calcite grains become elongate or form elongate aggregates with some large relic grains exhibiting microfractures, preferentially oriented at ca. 45° to the sense of shear. Grain boundaries start to show lobate geometry. There is also a dramatic reduction in grain size of the calcite, by dynamic recrystallization, to form narrow trains and aggregates of finely recrystallized calcite (Fig. 4(b)). These become interconnected thin layers (thickness 10–100 μm) of small calcite grains that cross-cut the sample forming discrete bands oriented at small angles (ca. 45°–30°) with respect to the shear direction (cf. Fig. 4(c) and (d)). Some of these interconnected bands show anastomosing geometries (Fig. 4(d)) they appear to develop where the maximum strain accrued and are not necessarily in the centre of the sample (cf. Fig. 3). Along the margins of the more prominent bands of recrystallized calcite are small microfractures (white arrow in Fig. 4(b)).

Muscovite crystals between the calcite rotate to orient their c-axes towards the shear direction, defining a clear S-foliation at the sample scale (Fig. 4). At lower strains the muscovite is extensively

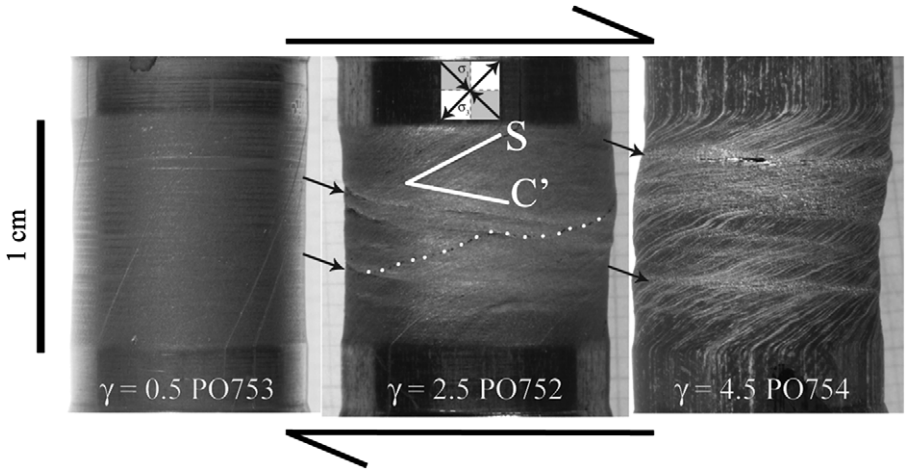

Fig. 3. Photographs of three deformed specimens inserted in the iron jackets. The large arrows indicate the sense of shear, the bulk shear strain and experiment numbers are given for each sample. S-planes are parallel to the inclined strain markers (highlighted in white); small black arrows indicate the orientation of the C′ folia. Note the hole in the iron jacket (PO754) occurring within one of the C′ planes.

bent and kinked and defines an imperfect foliation (Fig. 4(a)). Kinking is common in the lower strained portion of the samples with kink-bands having wavelengths on the order of 5 μm, with their axial traces at ~40° to the foliation trace and overturned in a manner consistent with the shear sense. At higher strains the muscovite can be tightly folded and individual grains, particularly those lying in the shear direction, can be boudinaged (Fig. 4(f)). The boudins necks and the margins of the muscovite appear to be covered by a reaction product that is probably akin to the dehydroxylation-breakdown of muscovite described by Mariani et al. (2006).

At $T = 727$ °C and bulk shear strains $\gamma > 2$, similar microstructures were observed in all samples to the 627 °C experiments despite slower strain rates (Fig. 5). However, a slight increase in the grain size of the recrystallized calcite that defines the foliation was observed. Comparing specimens from $\gamma = 2.5$ (Fig. 5(c) and (d)) with those deformed at higher shear strains (Fig. 5(e) and (f)) there is also a noticeable increase in shear band development and the muscovite becomes intensely kinked (Fig. 5(e)) and folded. There is also a noticeable increase in the number of fractures adjacent to the zones of finely recrystallized calcite (Fig. 5(f)).

Catastrophic failure systematically occurred in all specimens where the shear strain was exceeded by $\gamma > 2$. This failure is also at sites that correspond to the zones of strongest calcite localization in the shear bands and to sites where the brittle fractures were observed in the microstructure; with an orientation resembling that of R_1 Riedel shears (Logan et al., 1992). However, the location of these dilatant fractures was difficult to identify in thin section but can be clearly seen on polished sections of the specimen or in SEM images (Fig. 8). The microstructural features imply that both crystal-plastic and brittle processes are occurring together and contributed to the overall deformation of these specimens. Dilation is associated with the creation of openings parallel to (001) planes in muscovite (Fig. 8(a) and (b)) and fracturing along the planes of calcite localization (Fig. 8(b)–(e)),

3.4. Crystallographic preferred orientation (CPO) in calcite

The calcite CPO of representative calcite–muscovite samples was analysed using the microfabric analyser described by (Wilson et al., 2007). The CPO of the starting material is weak (Fig. 1(b) and (c)) as is illustrated by the cumulative misorientation angle of the c-axes, displayed using a histogram that shows the deviation of the c-axes from a random c-axis distribution (solid line in Fig. 1(d)). There is also a slight tendency to have c-axes spread around the shortening direction, which is perpendicular to the mica fabric. The latter is assumed to be created by twinning during cold-pressing, which rotates the c-axes towards the maximum shortening direction. The subsequent hot isostatic pressing does not change the principal shape of the texture (e.g. Barnhoorn et al., 2005).

At shear strains of $\gamma = 1$ (Fig. 6), the foliation begins to become curved as shear bands or C′ planes begin to initiate (Fig. 6(a)) and two obvious calcite grain populations are observed. Large elongate (20–150 μm in length) old calcite grains with aspect ratios of approximately 1:5 that display extensive subgrain development and undulose extinction. Bounding the margins of these grains are small recrystallized grains (<15 μm) that become particularly abundant where the foliation is bent (Fig. 6(a)). The CPO of the large old grains generally reflects that of the starting material, a spread of c-axes at a high angle to the foliation (Fig. 6(b)). On the other hand the c-axes orientation of the recrystallized grains are broadly scattered, but with a marked concentration at a high angle to the C′ planes and perpendicular to the foliation S (Fig. 6(c)). There is also a non-reproducibility of data between the large grains (Fig. 6(b)) and adjacent finer grained areas (Fig. 6(c)).

In the higher strained samples, where there has been extensive localization (segregation?) of the calcite (Fig. 7(a)–(c)) the CPO begins to deviate markedly from a random pattern (Fig. 7(d) and (f)). This strengthening of the pattern is particularly noticeable in areas of higher strain (Fig. 7(g) and (h)) with distinct double maxima inclined at about ±45° to the shear direction and at ±60° to the shear plane and an overall orthorombic symmetry of the distribution (Fig. 7(d)). In isolated shear bands (Fig. 7(f)) populations of recrystallized grains have a distinct CPO with the maxima aligned normal to the shear direction and at ±60° to the shear plane (Fig. 7(g)). This pattern is typical of the CPO identified in similar torsion experiments performed on Carrara marble (Barnhoorn et al., 2004; Pieri et al., 2001).

3.5. Porosity evolution

The initially high porosity (20%) of the starting material is dramatically reduced during the cold pressurization of the samples to approximately 240 MPa preceding the temperature ramping to target conditions in the Paterson rig. Few specimens were unloaded right after pressurization due to gas leaking problems and analysed

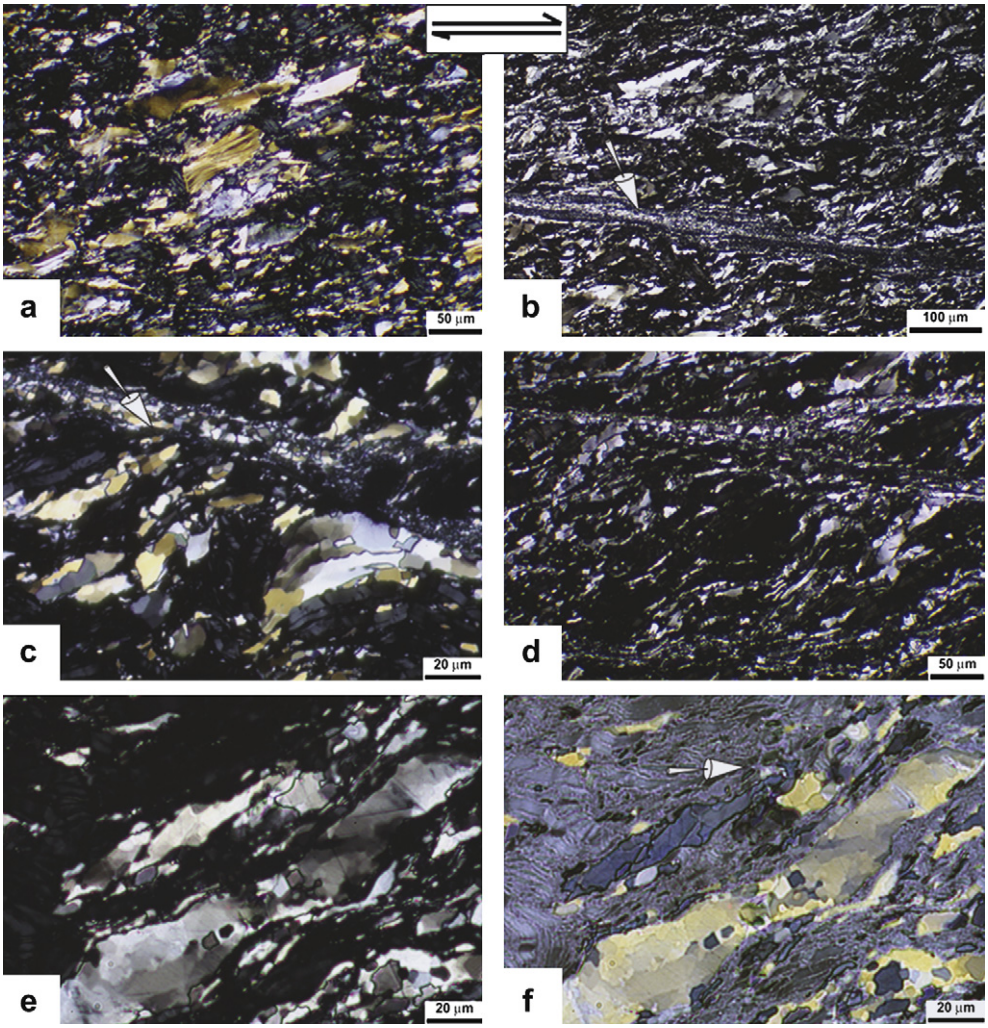

Fig. 4. Microstructures at $T = 627$ °C, shear strain rate 6×10^{-5} s^{-1} and shear strains of $\gamma = 1$ (a, sample PO778) and $\gamma = 3$ (b–f, sample PO783). The sense of shear is dextral in all micrographs. (a) At low shear strains there is extensive twinning and subgrains formation within calcite grains and elongation into lens shaped aggregates defining the foliation. Muscovite grains are iso-aligned with the long axis defining the foliation (polarized light image). (b) The relict calcite in the regions adjacent to the zones of strain localization has twins with lobate boundaries and is transitional into subgrains and a mantle of recrystallized grains (polarized light image). Transecting the foliation are zones of finely recrystallized calcite that may be bounded by dilatant fractures (white arrow) (c and d). Microstructure typical of the central region of the specimen where the foliation becomes curved into spaced zones of finely recrystallized calcite that is localized as elongate lenses in the shear bands (c) or bifurcates into anastomosing shear bands (d). (e) Polarized light image illustrating the elongate and recrystallized calcite with the preferentially aligned muscovite grains defining the foliation. (f) Plane polarized light image of the same area as (e) that illustrates the folded muscovite grains between the calcite. The muscovite is boudinaged (white arrows) and reaction products are observed in the boudin necks and adjacent to the muscovite.

under the SEM. A first order analysis of the BSE images revealed a residual porosity of approximately 5%. Furthermore specimens which underwent deformation but were recovered before catastrophic failure show an even smaller porosity of the order of 3–4%. With this analysis we could not find a relationship between the amount of strain witnessed by the sample and the resulting porosity.

3.6. Reaction and phase identification

Samples prepared by hot pressing at high temperature (670 °C) and deformed under axial compression (627 °C) show no microstructural evidence of reaction between the calcite and muscovite. This was supported by SEM imaging and microprobe investigations that revealed there was no variation in composition with respect to the staring material (Fig. 8).

On the contrary, all specimens deformed in torsion (627–727 °C) analysed under the SEM show the presence of some reaction products. The new phases mainly occur at the interfaces between calcite and muscovite and in dilational sites within the muscovite grains, such as boudin necks or in hinges of folded grains, where adjacent (001) cleavages become widely spaced (Fig. 8(a) and (b)). The reaction products were recognized by identifying X-ray diffraction peaks obtained from small quantities of ground powders of the deformed samples (Fig. 8(c)). The analysis revealed the coexistence of the reactants calcite and muscovite with the products anorthite and kalsilite in agreement with what is predicted by phase equilibria calculated using Perplex (Connolly, 1990) and the published thermodynamical database (Holland and Powell, 1998). Elemental mapping based on the characteristic X-ray radiation was used to visualize the spatial distribution of selected elements. The images show minor zonation in terms of Al and K in the muscovite crystals with the highest concentrations at the inner part of the grains. In addition the elemental maps clearly show that the C' oriented shear zones are mainly composed of calcite as Ca is the only traceable element within such planes (Fig. 9).

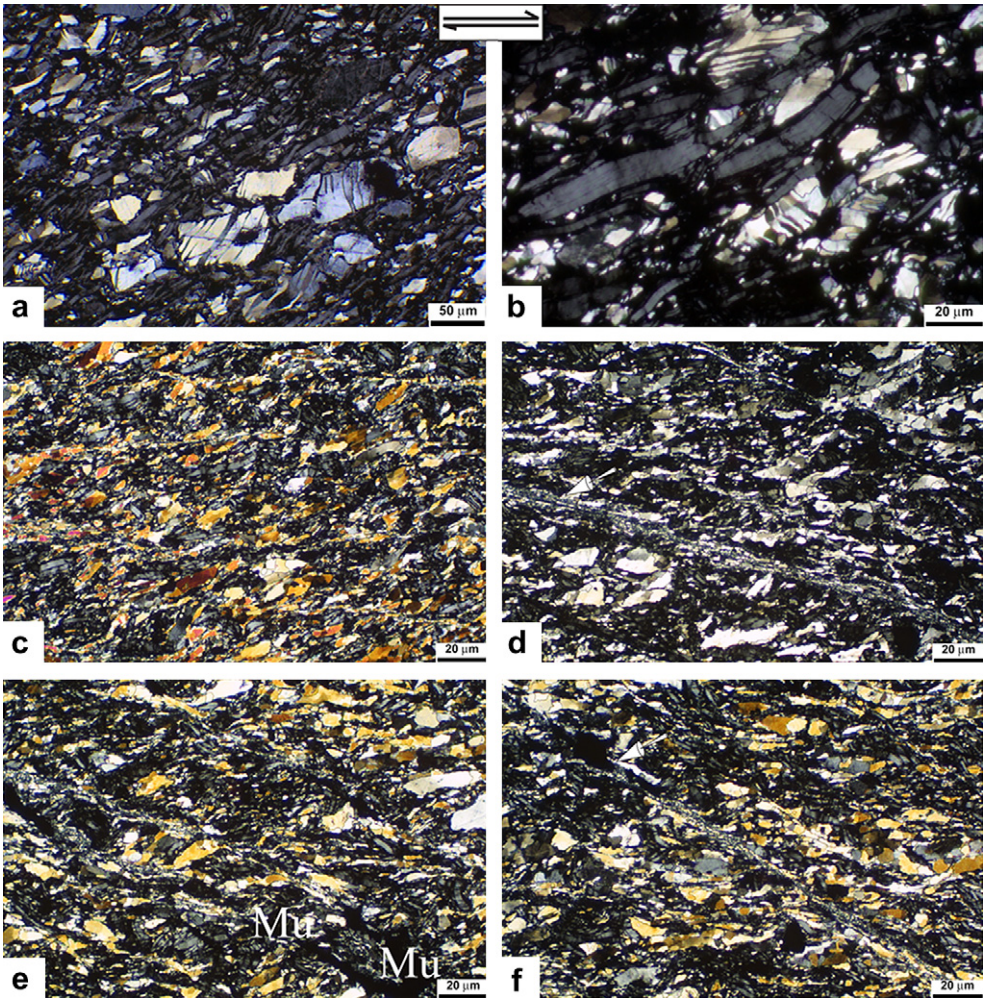

Fig. 5. Microstructures at $T = 727$ °C, shear strain rate 3×10^{-4} s^{-1} and $\gamma = 0.5$ (a and b, sample PO753); shear strains of $\gamma = 2.5$ (c and d, sample PO752) and $\gamma = 4.5$ (e and f, sample PO754). Photomicrographs in crossed polarized light, the sense of shear in all micrographs is dextral. (a and b) At low strains calcite grains are twinned and tend to assume a weak shape preferred orientation with the long axis inclined towards the shear direction. Muscovite grains are gently bent or kinked and preferentially aligned with the long axis defining the foliation. (c) The initiation of shear band localization in a lower strained section of specimen that contains coarse recrystallized calcite. (d) Shear bands from a marginal region of the specimen composed of fine recrystallized calcite transecting a foliation defined by elongate aggregates of recrystallized calcite. On its margin there is also a dilatant fracture (white arrow). (e) Sample with larger shear strain ($\gamma = 4.5$) where shear bands separate zones of deflected foliations that contain highly deformed and kinked muscovite aggregates (Mu). The axial surface for the majority of the kinks is aligned in the direction of the shear bands. (f) A prominent shear band, dominated by fine recrystallized calcite that also contains a dilatant fracture on its margins (white arrow).

4. Discussion

4.1. Mechanical evolution and deformation mechanisms

The torsion experiments show a rather complex stress–strain pattern that can be correlated with the microstructural evolution that progressively develops during shear strain. The initial quasi-linear elastic loading can be attributed to pore collapse of the aggregate. Samples that underwent small shear strains showed a homogeneous volume reduction and increase in density of up to 20% respect to the non-strained material. It has been shown elsewhere (Corkum and Martin, 2007) that closure of existing porosity results in an unusual non-linear mechanical response at very low strain and stress levels. This could explain the lower porosity of the strained samples with respect to those pressurized at isotropic conditions.

The post yielding-hardening region of the stress–strain curves microstructurally corresponds to the rotation of the mica crystals, which tend to be reoriented towards the imposed flow direction and become folded and kinked. Many of the muscovite grains are intensely kinked with microfracturing and dilation parallel to (001) and kink band boundaries; therefore dislocation glide on (001) must be active as described by Bell et al. (1986).

Whereas, intragranular deformation takes place within the calcite grains in the form of twinning, subgrain formation, with dynamic recrystallization and grain boundary migration. Dislocation movement along the activated slip systems results in a crystallographic preferred orientation at high strains. The main features of such fabric in terms of c-axis measured on the deformed calcite–muscovite aggregates, are comparable (Fig. 7) with those observed on pure calcite marble and can be explained with the activity of the high temperature slip systems {c} <a> and {r} <a> (Pieri et al., 2001; Barnhoorn et al., 2004; Romeo et al., 2007).

High-temperature experiments performed on pure muscovite (Mariani et al., 2006), showed that in absence of recovery processes the semi-brittle behaviour of muscovite, accompanies heterogeneous plastic deformation (kinking, folding and fracturing) leading to significant strain hardening that prevented the specimen reaching a mechanical steady-state. A similar but less pronounced behaviour is also observed during large-strain experiments on pure

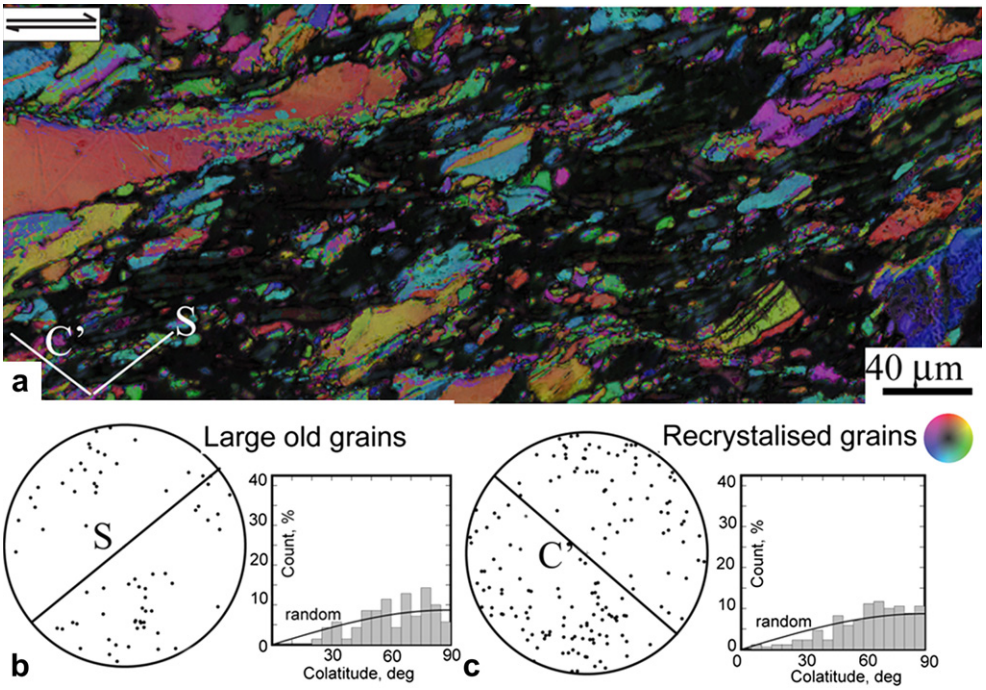

Fig. 6. AVA image and c-axis fabrics related to experiment PO778 ($\gamma \sim 1$; $T = 627$ °C). (a) AVA map that illustrates a microstructure dominated by the foliation defined by old calcite grains aligned in the muscovite foliation (S) that is deformed along C′ planes. At the bottom right of the map is a colour code that relates the three-dimensional c-axis orientation, namely the azimuth and plunge of the c-axis at each pixel seen in the AVA image. (b) Lower hemisphere equal area stereonet plot showing the distribution of c-axes and number (N) of large old grains analysed. The corresponding histogram shows frequency of grains whose c-axes occur at angle θ to the c-axis of adjacent grain, the curve represents a random distribution of c-axes. (c) Lower hemisphere equal area stereonet and histogram plot showing the distribution of c-axes and number (N) of large recrystallized grains analysed.

Carrara marble; for relatively small shear strains calcite shows pervasive intracrystalline deformation that is linked to a slow hardening of the marble as it undergoes deformation (Pieri et al., 2001; Barnhoorn et al., 2004). Given that in both calcite and muscovite high-temperature dislocation creep may be active at the investigated temperatures, we attribute the strain hardening behaviour observed in our torsion experiments, to the numerous phase boundaries present in the aggregate acting as obstacles to the dislocation motion and thus preventing recovery processes.

The following weakening (up to more than 60% with respect to the peak stress) during the high-strain tests is concomitant with the onset of recovery processes in the calcite crystals: dynamic recrystallization of the internally strained grains and the nucleation of small strain-free grains, which tend to align and interconnect forming thin and continuous planes oriented at small angles against the shear direction. Ultimately the strength of the aggregate is only controlled by that of calcite deforming via dislocation creep. This is strongly suggested if a comparison is made of the stress–strain curves obtained from pure Carrara marble and calcite + muscovite aggregates experimentally deformed at the same temperature and strain rate conditions (Fig. 2(a)). After significant weakening the shear strength of the synthetic aggregate reaches a quasi-steady-state value that overlaps the high-strain strength of pure Carrara marble.

4.2. Strain localization and competence contrast

Several microstructural features indicate that at the experimental conditions investigated here a significant competence contrast exists between calcite and muscovite. As illustrated above several, muscovite grains are boudinaged, indicating that mica is more competent than calcite with the latter being able to plastically accommodate strain in an easier fashion. Moreover the high-strain experiments show that dynamic recrystallization of the calcite grains results in the formation of an interconnected network forming a continuous compositional layering where shear strain localizes. The localization process results in the formation of S–C′ fabrics. The foliation plane (S) is defined by the long axes of the muscovite grains. The shear plane (C′) becomes evident at large bulk strain ($\gamma > 1$) and is characterized by zones of fine-grained dynamically recrystallized calcite crystals. Sample- and micro-scale examination reveal that the foliation (S) is displaced by the C′ shears indicating that the latter formed in a later stage than the first in agreement with field-based observations in mylonitic rocks (Platt and Vissers, 1980).

4.3. Cavitation at high strains

The samples deformed in torsion at shear strains greater than $\gamma \sim 2.5$ show the development of abundant pores and cavities that are initiated in different ways. An intergranular set of voids adjacent to the recrystallized calcite grains or small-scale fractures grows in length and connects to become larger fracture sets. Ongoing deformation promotes the interconnection of pores and voids into straight open cavities that eventually rotate into a stable orientation and develop fractures oriented at small angle against the sense of shear (Fig. 10(c) and (d)). The dilatant fractures proliferate in the regions of calcite localization and truncate the pre-existing fabric (Fig. 10(e)). Catastrophic failure eventually occurs in the specimen as a result of the development of major fracture cutting through the outer surface of the specimen (Fig. 10(f)).

Intracrystalline cavities also form within the deformed muscovite grains undergoing basal slip (Fig. 10(a)) similar to the observations of Bell et al. (1986). Intragranular fracturing must also be occurring in the muscovite to produce the fracture boudinage

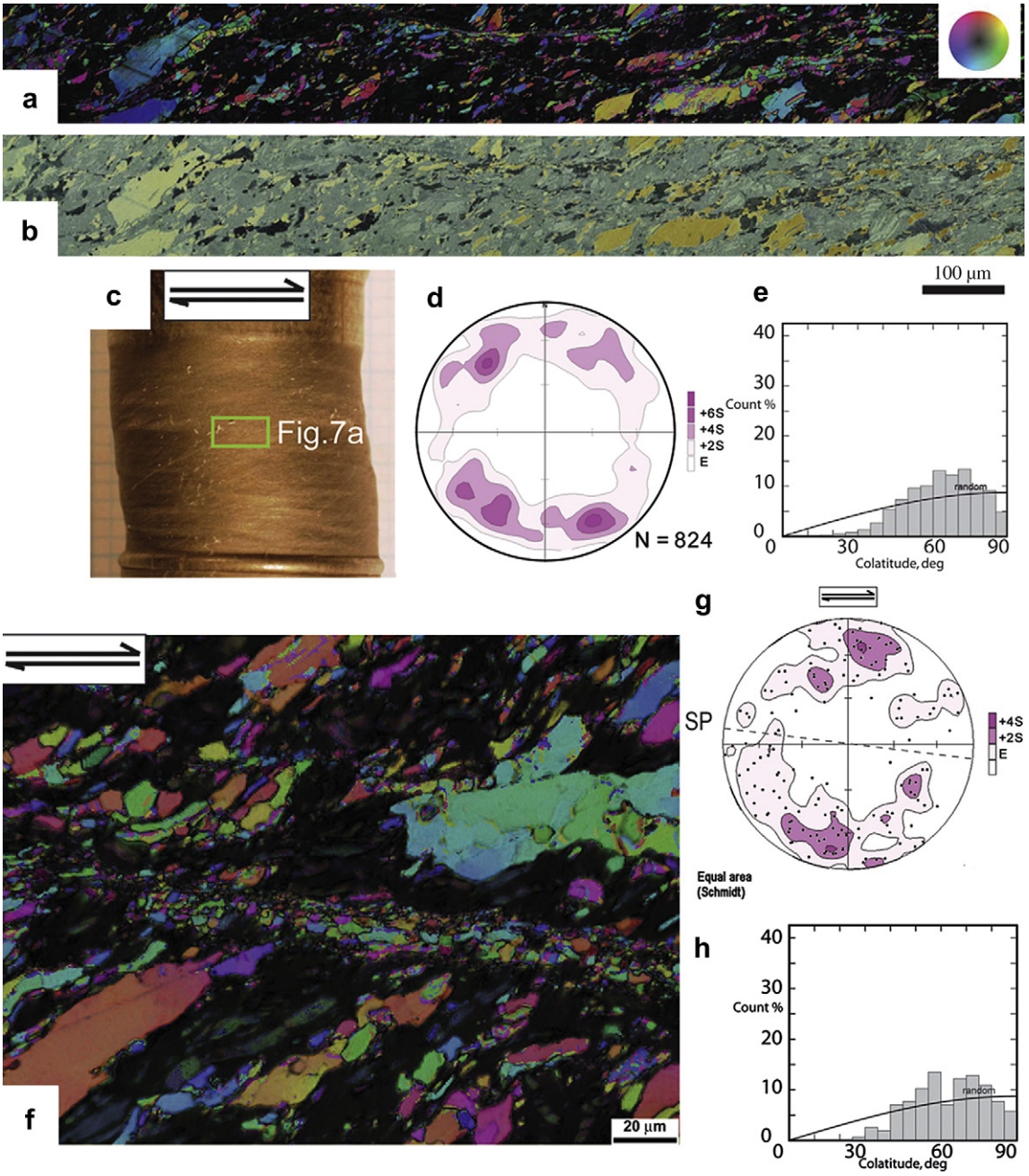

Fig. 7. AVA image and c-axis fabrics related to experiment PO783 ($\gamma = 3$; $T = 627$ °C). (a) AVA map that illustrates a localization of the new recrystallized calcite grains into shear bands that cross-cut the foliation (S) defined by the alignment of large relict calcite grains. The colour wheel relates the three-dimensional c-axis orientation, namely the azimuth and plunge of the c-axis at each pixel seen in the AVA image. (b) The same area as (a) viewed in plane polarized light. (c) Steel jacket of deformed sample and approximate location of area shown in (a). Lower hemisphere equal area stereonet plot showing the distribution of c-axes and number (N) of data points analysed. (d) Histogram showing frequency of grains whose c-axes occur at angle θ to the c-axis of adjacent grain, the curve represents a random distribution of c-axes. (f) AVA image showing distribution of orientations across a zone of calcite localization. (g and h) Distribution of c-axes and frequency distribution of the small recrystallized grains measured in (f).

observed in the muscovite. Cavitation, formation of submicroscopic cavities is driven primarily by glide on one slip system and the generation of dislocations that leads to kinking and dilatancy to accommodate deformation in the muscovite (Bell et al., 1986). This must represent a localized positive volume change. Moreover micropores along the (001) planes probably represent a dehydration reaction in the muscovite; a relatively high porosity can be observed in the SEM images of the highly strained specimens at the phase contacts between calcite and muscovite (Fig. 10(b)). A close examination of individual calcite grains also revealed the presence of sets of thin, almost rectilinear, regularly spaced intragranular fractures. Those fissures occur preferentially in an orientation oblique to the shear direction, roughly parallel to the direction of the maximum principal stress σ_1. Since they do not show any evidence of rotation or strain sensitive orientation we interpret them to be late features likely associated with the sudden pressure drop arising from the catastrophic failure of the specimen.

According to the proposed models (Kassner and Hayes, 2003; Chokshi, 2005; Zavada et al., 2007) cavitation results from the coalescence of intergranular microvoids and intragranular fractures

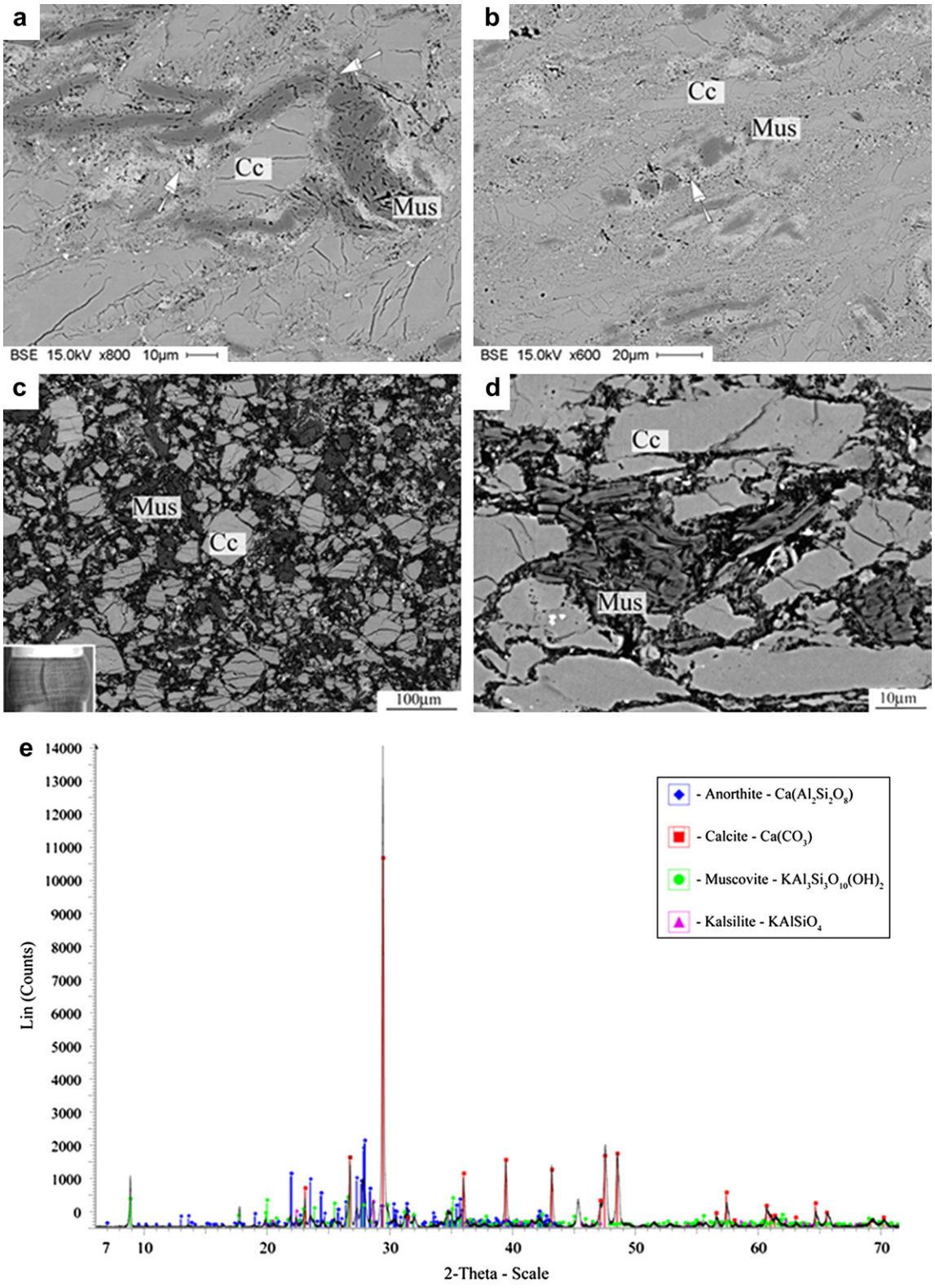

Fig. 8. (a) BSE SEM images of a sample deformed in torsion (PO754) showing Cc = calcite (light phase) and Mus = muscovite (dark phase). Muscovite grains are folded and kinked. White arrows indicate the occurrence of mixed reaction products (anorthite and kalsilite) in intracrystalline dilational sites and adjacent to the muscovite. (b) Boudinaged muscovite (dark grains) with reaction products in the boudin necks (see arrow). (c) BSE SEM image of microstructure from the axially compressed specimen (PO876) characterized by a lack of reaction products. The insert shows the deformed sample within the iron jacket. (d) High magnification image showing no reaction between Cc and Mus in compression experiment. (e) X-ray diffraction peaks from a specimen deformed in torsion indicating the presence of coexisting anorthite, calcite, muscovite and kalsilite.

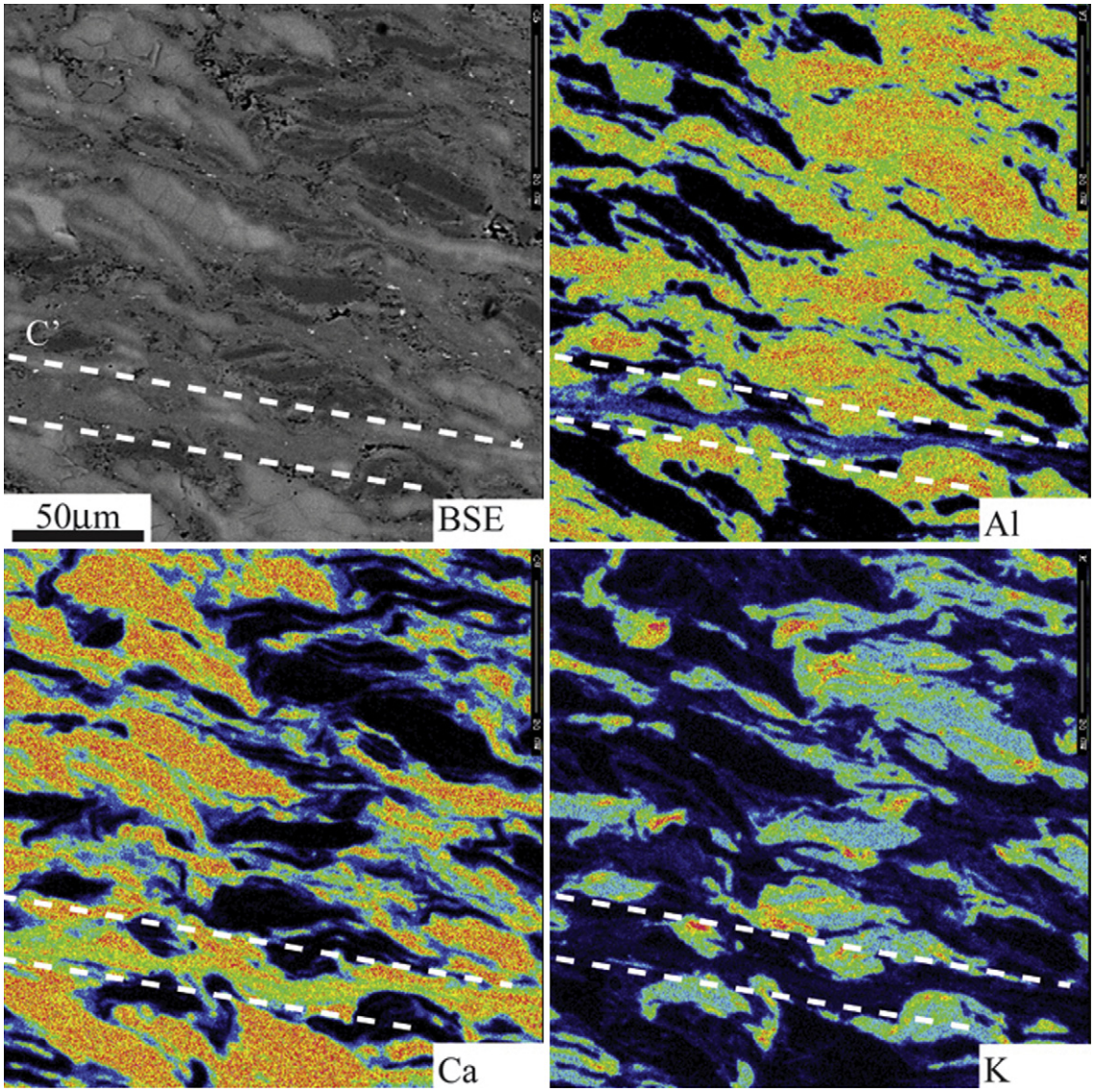

Fig. 9. X-ray elemental maps of the outer surface of a deformed specimen (PO752) obtained for selected elements (Al, Ca, K); BSE image in the upper left corner for reference. Sense of shear is dextral. In each map the warmest colours indicate a highest concentration of the mapped element. The dashed white lines highlight the occurrence of a C′ plane of localized strain, enriched in Ca but lacking of K and Al. Muscovite grains display a weak zonation of Al with the highest concentration towards their inner zones. K appears to be concentrated at the boundaries between calcite and muscovite grains reflecting the occurrence of reaction product kalsilite.

and produces local underpressures. The volume of the system increases due to creation of voids in muscovite and the grains support the voids as a load bearing framework, which soaks up the H_2O produced from the dehydroxylation reactions. We consider the "cavitation" model to be the most likely mechanism explaining the dilation, microfracturing and preferential distribution of reaction products to the highest strain areas and dilation sites within the specimens.

4.4. Mineral reactions at higher temperatures

Our observations suggest that there are complex interactions between deformation and mineral reaction particularly when there are positive volume changes that accompany the dilation. The densification of the starting materials, and accompanying negative volume change, was done at a temperature of 670 °C and 170 MPa and no reaction could be observed during the subsequent microstructural investigation (cf. Schmidt et al., 2008). In this study the samples were deformed at an even lower temperature (627 °C) with reactions producing new phases (ca. 10% volume) identified by XRD analyses as anorthite and kalsilite in agreement with thermodynamically calculated phase equilibria (Connolly, 1990). SEM images (Figs. 8 and 10) reveal that the new phases formed during torsion experiments, preferentially nucleated in dilation sites within muscovite grains such as hinges of folds or boudins necks in agreement with what is observed in naturally deformed muscovite (Wilson and Bell, 1979). Several interpretations could be put forward to explain these observations: the semi-brittle behaviour of the muscovite eventually results in the breakage of chemical bonds that releases water, which acts as a catalyst for the exchange reaction. It has also been suggested that deformation itself may add a component of kinetic energy to the system that could overstep the energy barrier of a chemical reaction (e.g. De Ronde and Stunitz, 2007). Here we also consider the role of the magnitude of the three main stress values and their evolution during torsion.

Fig. 11 illustrates the experimental conditions in a P–T diagram of muscovite and calcite in excess of water calculated using the

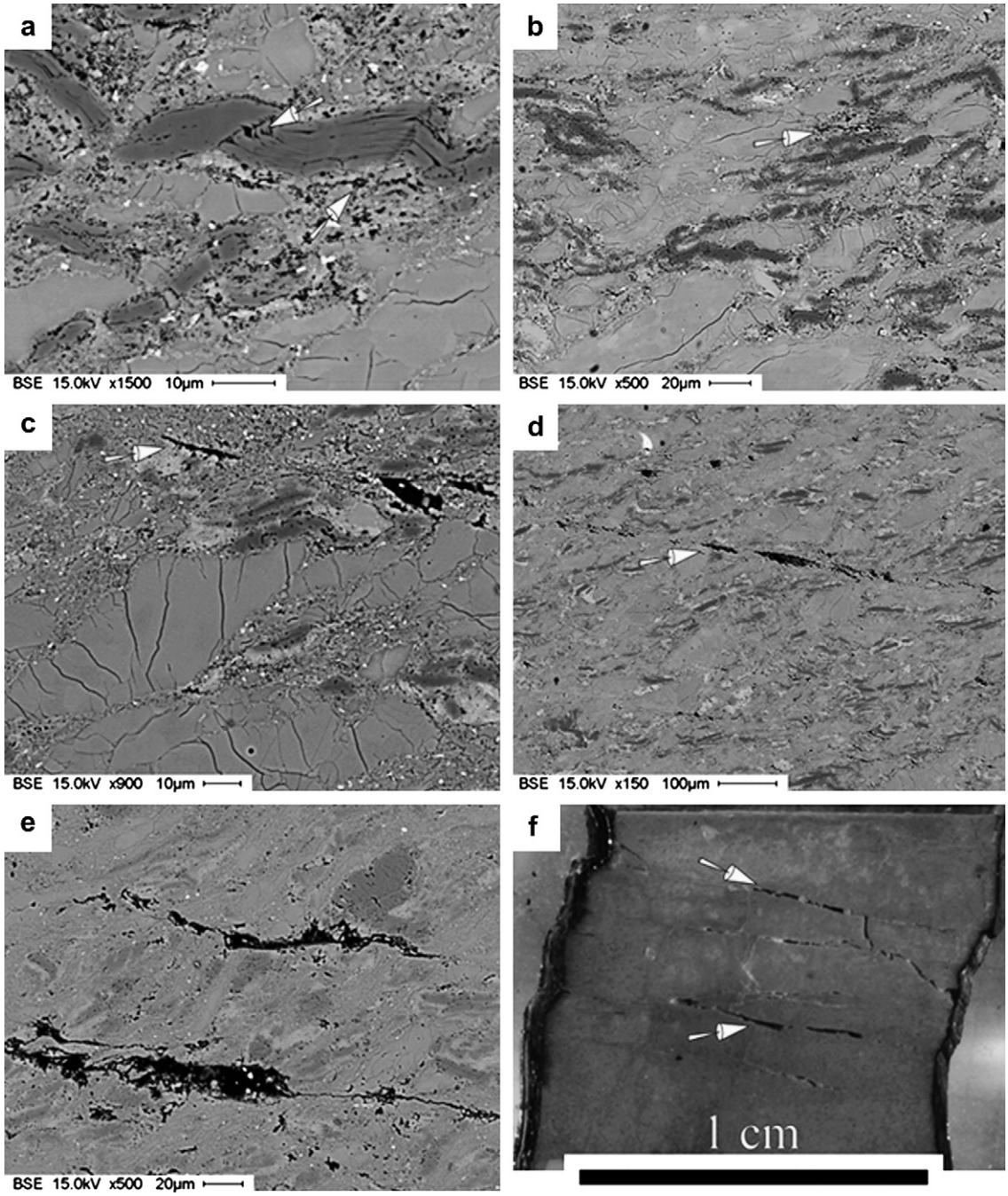

Fig. 10. Features associated with the distribution and evolution of dilatant fractures. Shear sense is dextral in all images. (a–e) SEM micrographs from PO754 ($\gamma = 4.5$). (a) The muscovite (darker phase) is kinked and folded. The hinges of the folded muscovite crystals show dilational sites and voids (white arrows) and the edges are surrounded by a reaction phase (light phase). (b–d) Muscovite surrounded by reaction phases and presence of small dilatant fractures (white arrows). (c) Note also the presence of small intragranular fracture within the calcite crystals preferentially oriented at about 45° against the shear direction. (e) Micrograph illustrating elongate trains of fractures that cross-cut the pre-existing fabric. (f) Fractures in tangential section (parallel to twist axis) sample PO752 after a shear strain $\gamma = 2.5$.

Perplex software (Connolly, 1990). The experiments conducted at 627 °C are in the stability field of calcite and muscovite, while those at 727 °C are in the stability field of anorthite, kalsilite, leucite and corundum. During compression and hydrostatic tests at 627 °C no reaction occurred, but during torsion testing, the muscovite reacted to produce anorthite and kalsilite.

We propose that during torsion, the minimum principal stress is controlling the conditions of reaction rather than the mean stress, because in torsion the mean stress remains unchanged with respect to hydrostatic conditions.

During creep deformation of rocks obeying a von Mises type of constitutive behaviour the magnitude of the three principal stresses will differ depending on the geometry of deformation (e.g. Paterson and Olgaard, 2000). In the case of torsion $\sigma_1 = p + \tau$; $\sigma_2 = p$ and $\sigma_3 = p - \tau$; while in axial compression $\sigma_1 = \sigma + p$; $\sigma_2 = \sigma_3 = p$; where p is the confining pressure, τ the shear stress and σ is the differential stress (σ_1–σ_3). The peak shear stress during torsion experiments performed at 627 °C was about 120 MPa. This means that the maximum compressive stress was equal to the confining pressure + the shear stress (300 + 120 MPa), whilst the minimum

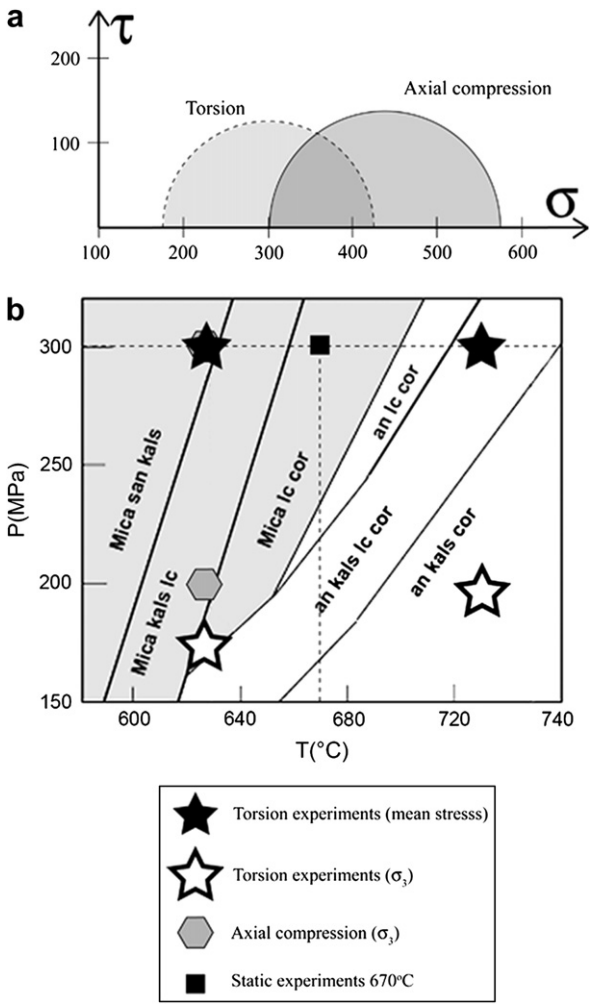

Fig. 11. (a) Mohr diagram illustrating the position of the maximum and least principal stresses in torsion and axial compression experiments performed at 627 °C. The magnitude of the stresses is derived following Paterson and Olgaard (2000) (see text for details). (b) Phase diagram calculated using Perplex (Connolly, 1990), overlayed are the conditions attained during torsion, axial compression and hydrostatic experiments. Note that during the torsion experiments at 627 °C, the least principal stress (σ_3) plots at the boundary between the fields defining the stability of the muscovite.

was $300 - 120 = 180$ MPa. These conditions corresponds roughly to the reaction muscovite = An + Kals (Fig. 11(a) and (b)).

This interpretation is in agreement with previous experimental evidence of growth of cristobalite fibers parallel to the direction of σ_3 in extension experiments (Brodie and Rutter, 2000) and in torsion tests (Schmocker, 2002) at conditions where the mean stress was well within the quartz stability field. No theoretical explanation yet exists to describe this behaviour. Based on microstructural observations we can argue that under dynamic conditions extension sites are preferential loci that favour the mobility of elements and the growth of minerals. Dilation sites act as surfaces where surface energy and tendency of anisotropic growth of the new phases overcome the influence of pressure difference between the mean stress and σ_3.

Equilibration of this new mineral assemblage can only be achieved by intracrystalline volume diffusion, with recrystallization and mineral growth (Worley et al., 1997). However, as these experiments have demonstrated, pressure rather than temperature, appears to be a factor that controls whether volume diffusion will be a significant process. Also critical is the magnitude of the shear strain as the changing chemical and decreasing stress conditions only become obvious at shear strains greater than 2. At this stage grain boundary fluids related to dehydroxylation reactions and the breakdown of muscovite release water contemporaneously with the crystal-plastic deformation. This is accompanied by the neocrystallization of the new phases that are localized along (001), boudin necks, grain boundaries and voids in the muscovite.

5. Geological implications

Even though strain partitioning is commonly observed in naturally deformed rocks, the mechanisms through which deformation localizes and phase segregation is attained are not well understood (e.g. Platt and Vissers, 1980; Passchier, 1991: Worley et al., 1997). From our experiments we infer that a strong foliation is a prerequisite for the formation of the secondary C′ type shear band. The development of the latter is contemporaneous with the onset of dynamic recrystallization and the attainment of a new fabric in the calcite grains which in turn induces a strain softening in the deforming aggregate. It therefore appears that the development of an S–C′ foliation is a mechanically favourable arrangement during the deformation of polyphase material exhibiting competence contrast between the two phases.

Since calcite and muscovite possess very different crystallographic structures, and slip systems, their rate in accommodating deformation will be different. It has been experimentally shown that pure Carrara marble deforms up to extremely large strains ($\gamma = 50$, Barnhoorn et al., 2004) without any evidence for strain localization. In the current experiments localization occurred in the calcite at bulk shear strains as low as $\gamma = 2$ with the subsequent development of dilatant fractures at these sites. The genesis and growth of such fractures are associated with the presence of microvoids due to the dehydration of muscovite, and to the differential rate of movement and deformation of the two phases. Eventually the evolving dilatant fractures produced a catastrophic loss of cohesion in the aggregate. A similar process has been observed in aggregates of anorthite–diopside (Dimanov et al., 2007) experimentally deformed to large strain during linearly viscous creep and in various studies on metals, ceramics and alloys (Pilling and Ridley, 1989; Nieh et al., 1997; Kassner and Hayes, 2003). All these previous studies suggest that the cavitation process would lead to a shortening of the "ductility" in the investigated material.

The question arises whether the cavitation process could be active in nature during deformation of rocks and what its consequences would be? Several field-based studies of mylonitic rocks have reported the presence of voids, vugs or cavities within highly strained portions of the rock body. Behrmann and Mainprice (1987) recognized small elliptical voids decorating quartz grain boundaries in an orthomylonite deformed under amphibolite grade conditions; the voids were interpreted as tensional grain boundary failure. Fine isolated intergranular pores and millimetre scale vug-like cavities have been recognized in retrograde quartz mylonites preferentially concentrated in extension surfaces (Mancktelow et al., 1998). Also a microstructural investigation of a fine-grained plagioclase shear zone from the Abukuma Mountains, Japan revealed the presence of intergranular voids and the development of a "crush zone" within layers of strong plastic deformation (Shigematsu et al., 2004). On a larger scale, finite element modelling was used to infer that in the tensile domain of the Alpine collision (Eifel volcanic zone), a small amount of dilatancy is created along shear bands in the upper mantle and lower crust in conditions were dynamic recrystallization and ductile deformation are active (Regenauer-Lieb, 1999).

All the examples cited above, suggest that a localized tensile behaviour of the plastically deforming rocks, has potential implications for deep fluid flow in the deforming lower crust and upper mantle, and may dictate the pathways for fluids, melts and gases and subsequent alterations and metasomatism of deeply seated rocks. Moreover plastic failure observations indicate that dynamic instabilities may nucleate at lower-crustal depth and may be responsible for deep earthquake nucleation.

The onset of reaction at conditions in which the pressure equals the σ_3 rather than the confining pressure or the mean stress poses serious questions on the utilization of mineral phase equilibria to syn-tectonic growth. It is possible that P, T estimations of metamorphic rocks underestimate real depths in cases similar to our experiments. Moreover a more general question may arise on the interpretation of P, T conditions in static versus dynamic conditions, since it is possible that dynamic conditions are totally different. Our experimental observations can be interpreted in two different ways:

1. Mineral reactions are displaced by differential stress
2. Minerals may grow in extension sites in "underpressure" conditions and hence be in equilibrium with σ_3 rather than with the mean stress.

The latter may imply that other minerals possibly form at sites of "overpressure" and hence be dominated by the σ_1 rather than by the confining pressure and the mean stress. More focused experiments are required to elucidate these possibilities that might shed new light on the interpretation of geothermobarometry.

6. Conclusions

We performed a set of large-strain experiments on a synthetic aggregate composed of equal amount of calcite and muscovite. Our observations suggest that:

- The mechanical strength of a highly sheared polyphase rock is ultimately controlled by the weakest phase forming continuous layers along C′ surfaces for simple shear.
- A starting material with a random distribution of the phases will reach this ideal low strength configuration by a mechanical redistribution and microstructural transformation of the phases during the initial transient stage of the deformation. During this initial period the strength is higher than the strength of the final textured rock.
- The mechanical characteristics, and the ultimate bulk strength of the material is predominantly a function of the mineral composition of the rock and the strength of each phase, and is strongly influenced by the deformation mechanisms in each mineral. Once a foliation has developed, the strain is concentrated within the calcite shear zones and the muscovite domains are not deformed further but rather passively rotated.
- The layers of highly localized strain show a distinct fabric suggesting that the dominant deformation mechanism did not change during strain partitioning; the deformation behaviour of the aggregate at large strain is therefore controlled by the dislocation creep of calcite.
- Void nucleation and interconnection is an active process during high-temperature plastic creep and may lead to loss of cohesion of the deforming material, with potential implication for enhanced fluid flow and earthquake nucleation.
- Phase equilibria are strongly affected by deformation: we observed that at the same conditions of temperature and confining pressure the onset of reaction was governed by the magnitude of the least principal stress σ_3.
- Microstructures related to intracrystalline deformation, indicate an increasing importance of volume diffusion and diffusive equilibration of mica with calcite at pressures where the least stress is less than the mean stress.

Acknowledgements

The starting material used in this study was prepared by Volkmar Schmidt. R. Hofmann is thanked for the technical support in the laboratory and for the maintenance of the experimental apparatus. We thank the Electron microscopy centre of ETH (EMEZ) for granting the access to the SEM, and F. Pirovino for the thin sections preparation. We are grateful to L. Zehnder and P. Bouilhol who helped with the XRD and microprobe analyses respectively. We sincerely thank J.-P. Burg, M. Herwegh, K. Kunze, N. Mancktelow, E. Mariani, S. Schmalholz for their valuable comments on this work. Critical reviews by E. Mariani, and T. Mitchell were greatly appreciated. Research was supported by ETH grant TH 1/03-3/2704.5 and Australian Research Council DP0773097. CJLW thanks ETH Zürich and J-P Burg for making his visit possible.

References

Barnhoorn, A., Bystricky, M., Burlini, L., Kunze, K., 2004. The role of recrystallisation on the deformation behaviour of calcite rocks: large strain torsion experiments on Carrara marble. Journal of Structural Geology 26, 885–903.

Barnhoorn, A., Bystricky, M., Kunze, K., Burlini, L., Burg, J.P., 2005. Strain localisation in bimineralic rocks: experimental deformation of synthetic calcite–anhydrite aggregates. Earth and Planetary Science Letters 204, 748–763.

Behrmann, J.H., Mainprice, D., 1987. Deformation mechanisms in a high temperature quartz–feldspar mylonite: evidence for superplastic flow in the lower continental crust. Tectonophysics 140, 297–305.

Bell, I.A., Wilson, C.J.L., Mclaren, A.C., Etheridge, M.A., 1986. Kinks in mica: role of dislocations and (001) cleavage. Tectonophysics 127, 49–65.

Brodie, K.H., Rutter, E.H., 2000. Rapid stress release caused by polymorphic transformation during experimental deformation of quartz. Geophysical Research Letters 19, 3089–3092.

Bruhn, D.F., Casey, M., 1997. Texture development in experimentally deformed two-phase aggregates of calcite and anhydrite. Journal of Structural Geology 19, 909–925.

Bruhn, D.F., Olgard, D.L., Dell'Angelo, L.N., 1999. Evidence for enhanced deformation in two-phase rocks: experiments on the rheology of calcite–anhydrite aggregates. Journal of Geophysical Research 104, 707–724.

Chokshi, A.H., 2005. Cavity nucleation and growth in superplasticity. Materials Science and Engineering A 410–411, 95–99.

Connolly, J.A.D., 1990. Multivariable phase diagrams: an algorithm based on generalized thermodynamics. American Journal of Science 290, 666–718.

Corkum, A.G., Martin, C.D., 2007. The mechanical behaviour of weak mudstone (Opalinus Clay) at low stresses. International Journal of Rock Mechanics & Mining Sciences 44, 196–209.

De Ronde, A.A., Stunitz, H., 2007. Deformation-enhanced reaction in experimentally deformed plagioclase–olivine aggregates. Contributions to Mineralogy and Petrology 153, 699–717.

Dimanov, A., Rybacki, E., Wirth, R., Dresen, G., 2007. Creep and strain-dependent microstructures of synthetic anorthite–diopside aggregates. Journal of Structural Geology 29, 1049–1069.

Etheridge, M.A., Hobbs, B.E., Paterson, M.S., 1973. Experimental deformation of single crystals of biotite. Contributions to Mineralogy and Petrology 38, 21–36.

Gottschalk, R.R., Kronenberg, A.K., Russell, J.E., Handin, J., 1990. Mechanical anisotropy of gneiss: failure criterion and textural sources of directional behavior. Journal of Geophysical Research 95, 21,613–21,634.

Handin, J., Higgs, D.V., O'Brien, J., 1960. Torsion of Yule marble under confining pressure. In: Griggs, D., Handin, J. (Eds.), Rock Deformation (A Symposium). The Geological Society of America Memoir, vol. 79, pp. 245–274.

Handy, M.R., 1994. Flow law for rocks containing two non-linear viscous phases: a phenomenological approach. Journal of Structural Geology 16, 287–301.

Handy, M.R., Wissing, S.B., Streit, L.E., 1999. Frictional-viscous flow in mylonite with varied bimineralic composition and its effects on lithospheric strength. Tectonophysics 303, 175–191.

Herwegh, M., Jenni, A., 2001. Granular flow in polymineralic rocks bearing sheet silicates: new evidence from natural examples. Tectonophysics 332, 309–320.

Holland, T.J.B., Powell, R., 1998. An internally consistent thermodynamic data set for phases of petrological interest. Journal of Metamorphic Geology 16, 309–343.

Holyoke III, C.W., Tullis, J., 2006. Mechanism of weak phase interconnection and the effects of phase strength contrast on fabric development. Journal of Structural Geology 28, 621–640.

Jordan, P., 1985. The deformational behaviour of bimineralic limestone–halite aggregates. Tectonophysics 135, 185–197.

Kassner, M.E., Hayes, T.A., 2003. Creep cavitation in metals. International Journal of Plasticity 19, 1715–1748.
Leiss, B., Molli, G., 2003. High-temperature texture in naturally deformed Carrara marble from the Alpi Apuane, Italy. Journal of Structural Geology 25, 649–658.
Logan, J.M., Dengo, C.A., Higgs, N.G., Wang, Z.Z., 1992. Fabrics of experimental fault zones: their development and relationship to mechanical behavior. In: Evans, B., Wong, T.F. (Eds.), Fault Mechanics and Transport Properties of Rocks. Academic Press, London, pp. 33–67.
Mancktelow, N.S., Grujic, D., Johnson, E.L., 1998. An SEM study of porosity and grain boundary microstructure in quartz mylonites, Simplon Fault Zone, Central Alps. Contributions to Mineralogy and Petrology 131, 71–85.
Mares, V.M., Kronenberg, A.K., 1993. Experimental deformation of muscovite. Journal of Structural Geology 15, 1061–1075.
Mariani, E., Brodie, K.H., Rutter, E.H., 2006. Experimental deformation of muscovite shear zones at high temperatures under hydrothermal conditions and the strength of phyllosilicate-bearing faults in nature. Journal of Structural Geology 28, 1569–1587.
Molli, G., Conti, P., Giorgetti, G., Meccheri, M., Oesterling, N., 2000. Microfabric studies on the deformational and thermal history of the Alpi Apuane marbles (Carrara marbles), Italy. Journal of Structural Geology 22, 1809–1825.
Nieh, T.G., Wadsworth, J., Sherby, O.D., 1997. Superplasticity in Metals and Ceramics. Cambridge University Press, Cambridge, 273 pp.
Passchier, C.W., 1991. Geometric constrains on the development of shear bands in rocks. Geologie en Mijnbouw 70, 203–211.
Paterson, M.S., Olgaard, D.L., 2000. Rock deformation tests to large shear strains in torsion. Journal of Structural Geology 22, 1341–1358.
Pieri, M., Burlini, L., Kunze, K., Stretton, I., Olgaard, D.L., 2001. Rheological and microstructural evolution of Carrara marble with high shear strain: results from high temperature torsion experiments. Journal of Structural Geology 23, 1393–1413.
Pilling, J., Ridley, N., 1989. Superplasticity in Crystalline Solids. The Institute of Metals, 214 pp.
Platt, J.P., Vissers, R.L.M., 1980. Extensional structures in anisotropic rocks. Journal of Structural Geology 2, 397–410.
Regenauer-Lieb, K., 1999. Dilatant plasticity applied to Alpine collision: ductile void growth in the intraplate area beneath the Eifel volcanic field. Geodynamics 27, 1–21.
Romeo, I., Capote, R., Lunar, R., 2007. Crystallographic preferred orientations and microstructure of a Variscan marble mylonite in the Ossa-Morena Zone (SW Iberia). Journal of Structural Geology 29, 1353–1368.
Rutter, E.H., 1974. The influence of temperature, strain rate and interstitial water in the experimental deformation of calcite rocks. Tectonophysics 22, 311–334.
Rutter, E.H., 1995. Experimental study of the influence of stress, temperature, and strain on the dynamic recrystallisation of Carrara marble. Journal of Geophysical Research 100, 24651–24663.
Rutter, E.H., Brodie, K.H., 1992. Rheology of the lower crust. In: Fountain, D.M., Arculus, R., Kay, R.W. (Eds.), The Continental Lower Crust. Elsevier, Amsterdam, pp. 201–267.
Rybacki, E., Paterson, M.S., Wirth, R., Dresden, G., 2003. Rheology of calcite–quartz aggregates deformed to large strain in torsion. Journal of Geophysical Research 108 (B2) 2089. doi:10.1029/2002JB001833.
Schmid, S.M., Paterson, M.S., Boland, J.N., 1980. High temperature flow and dynamic recrystallisation in Carrara marble. Tectonophysics 65, 245–280.
Schmidt, V., Burlini, L., Hirt, A.M., Leiss, B., 2008. Preparation of synthetic calcite-muscovite rocks with variable texture – an analogue to cataclasite fabrics? Tectonophysics 449, 105–119.
Schmocker, M., 2002. Rheology and Microfabrics of Quartz: Experimental Deformation in Torsion. PhD thesis, ETH Zurich Nr. 14587, 197 pp.
Shea, W.T., Kronenberg, A.K., 1993. Strength and anisotropy of foliated rocks with varied mica contents. Journal of Structural Geology 15, 1097–1121.
Shigematsu, N., Fujimoto, K., Othani, T., Goto, K., 2004. Ductile fracture of fine-grained plagioclase in the brittle-plastic transition regime: implication for earthquake source nucleation. Earth and Planetary Science Letters 222, 1007–1022.
Tullis, J., Wenk, H.R., 1994. Effect of muscovite on the strength and lattice preferred orientations of experimentally deformed quartz aggregates. Materials Science and Engineering A175, 209–220.
Wilson, C.J.L., Bell, I., 1979. Deformation of biotite and muscovite: optical microstructures. Tectonophysics 58, 179–200.
Wilson, C.J.L., Russell-Head, D.S., Kunze, K., Viola, G., 2007. The analysis of quartz c-axis fabrics using a modified optical microscope. Journal of Microscopy 227, 30–41.
Worley, B., Powell, R., Wilson, C.J.L., 1997. Crenulation cleavage formation: evolving diffusion, deformation and equilibration mechanisms with increasing metamorphic grade. Journal of Structural Geology 19, 1121–1135.
Zavada, P., Schulmann, K., Konopasek, J., Ulrich, S., Lexa, O., 2007. Extreme ductility of feldspar aggregates—melt-enhanced grain boundary sliding and creep failure: rheological implications for felsic lower crust. Journal of Geophysical Research 112 B10210. doi:10.1029/2006JB004820.